In *Advances in Plasma Physics Research, Volume 3* ISBN 1-59033-329-2
Edited by Francois Gerard, pp. 1-32

Modeling Network for Argon Glow Discharge Plasmas with Copper Cathode

Annemie Bogaerts and Renaat Gijbels,
University of Antwerp, Department of Chemistry,
Universiteitsplein 1, B-2610 Wilrijk-Antwerp, Belgium.
E-mail: annemie.bogaerts@ua.ac.be

Abstract

In this paper, an overview is given of the modeling network that we have developed for argon glow discharges with copper cathode, and the individual sub-models (i.e., Monte Carlo, fluid, heat transfer and collisional-radiative models) for the various plasma species are briefly described. The typical results that have been calculated with the models are summarized and illustrated with some examples. To check the validity of the models, comparison with experimental data is made, whenever available. The reasonable agreement shows that the models present a realistic picture of the glow discharge.

1. Introduction

Glow discharges and related plasmas are used in a wide range of application fields, ranging from the semiconductor industry and materials technology (for surface modification, etching and deposition of thin layers), over the laser, light and flat plasma display panel technology, to environmental and biomedical applications [1]. Another application field of glow discharges which is not so well-known to plasma physicists is in analytical spectrometry, for the chemical trace analysis of (mainly) solid materials. The material to be analyzed is then used as the cathode of the glow discharge (or the rf-powered electrode, in the rf-case), which is sputter-bombarded by energetic plasma species. The sputtered, analytically interesting, atoms arrive in the plasma where they are subject to collisions, of which excitation and ionization are the most important. The excitation collisions create excited atoms, which emit characteristic photons that can be detected with an optical emission spectrometer (glow discharge optical emission

spectrometry, GD-OES). The ionization collisions give rise to the formation of ions, which can be measured in a mass spectrometer (glow discharge mass spectrometry, GDMS) [2].

For good analytical practice, a thorough insight in the glow discharge processes is desirable. We try to obtain that by numerical modeling. We have developed a comprehensive two-dimensional modeling network for argon glow discharges, including the sputtered (copper) atoms and ions, operated in direct current (dc) mode, capacitively coupled radio-frequency (rf) mode and pulsed mode, at typical operating conditions used in analytical chemistry. However, the model is of course also applicable to glow discharges working at similar conditions but used in other application fields. In the following sections, the modeling network will be briefly described, and some typical results will be illustrated.

2. Description of the Modeling Network:

Different kinds of models have been developed in the literature to describe glow discharge plasmas, i.e., analytical approximations [3], fluid models [4], Boltzmann equations [5], Monte Carlo codes [6] and particle-in-cell simulations [7]. All these models have their specific advantages and disadvantages. For example, analytical and fluid approaches are in principle rather fast, but they are based on approximations, which are only valid for certain conditions. The solution of the full Boltzmann transport equation is more generally valid, but it can become mathematically very complicated. Monte Carlo and particle-in-cell simulations, on the other hand, are very accurate and mathematically simple, but they require a long calculation time. In order to combine the advantages of the various models and to get rid of the disadvantages, we have developed a hybrid modeling network consisting of various sub-models for the different plasma species. Table 1 gives an overview of the plasma species considered in our simulations, as well as the models used to describe these species. We assume that the discharge gas is pure argon and that the cathode is made of pure copper. The Monte Carlo simulations are carried out in three dimensions. The fluid model, the collisional-radiative models and the heat transfer model, on the other hand, are only developed in two dimensions (axial and radial direction), because of the cylindrical symmetry of the discharge cells under consideration. The various sub-models will be briefly described here.

2.1. Argon Gas Atoms: No Specific Model or Heat Transfer Model:

The argon gas atoms are usually assumed to be at rest, uniformly distributed throughout the discharge, and in general no model is used to describe their behavior. Nevertheless, we have also developed a model to describe argon gas heating in dc glow discharges, and we calculated a non-uniform gas temperature and hence a somewhat non-uniform argon gas density. The gas temperature is calculated as a function of z and r

position with the heat conduction equation:

$$\frac{\partial^2 T_g}{\partial z^2} + \frac{1}{r}\frac{\partial}{\partial r}\left(r\frac{\partial T_g}{\partial r}\right) = -\frac{P}{\kappa}$$

where T_g is the argon gas temperature, P is the power input, and κ is the thermal conductivity (= 1.8×10^{-4} W cm^{-1} K^{-1} for argon). The power input in the argon gas is calculated in the ion and atom Monte Carlo models (see below), based on collisions and subsequent energy transfer of the argon ions, fast argon atoms and copper atoms into the argon gas. A detailed description of this model can be found in ref. [8].

Table 1: Overview of the different plasma species considered in the simulations, and the various models used to describe these species.

Plasma species	Model
Ar gas atoms	no model (uniformly distributed + at rest) or: heat transfer model (dc case)
fast electrons	Monte Carlo model
slow electrons	fluid model
Ar^+, Ar^{2+}, Ar_2^+ ions	fluid model
Ar^+ ions in CDS	Monte Carlo model
fast Ar^0_f atoms in CDS	Monte Carlo model
Ar atoms in various excited levels	collisional-radiative model
sputtering of the Cu atoms	empirical formula
sputtered Cu atoms: thermalization	Monte Carlo model
Cu atoms and ions in ground state + excited levels	collisional-radiative model
Cu^+ ions in CDS	Monte Carlo model

2.2. Fast Electrons: Monte Carlo Model:

The electrons are split up in a fast and a slow group, depending on their energy. The electrons are called "fast" when they have enough energy to produce inelastic collisions (i.e., ionization and excitation of argon or copper). These fast electrons are not in equilibrium with the electric field, i.e., they gain more energy from the electric field than they lose by collisions. The most accurate way to describe their behavior is by means of Monte Carlo simulations.

A large number of electrons is followed, one after the other, during successive time-steps. During each time-step, the trajectory of an electron is calculated with Newton's laws:

$$z = z_0 + v_{z_0}\Delta t + \frac{qE_{ax}(z,r,t)}{2m}(\Delta t)^2$$

$$x = x_0 + v_{x_0}\Delta t + \frac{qE_{rad}(z,r,t)\cos(\alpha)}{2m}(\Delta t)^2$$

$$y = y_0 + v_{y_0}\Delta t + \frac{qE_{rad}(z,r,t)\sin(\alpha)}{2m}(\Delta t)^2$$

$$v_z = v_{z_0} + \frac{qE_{ax}(z,r,t)}{m}\Delta t$$

$$v_x = v_{x_0} + \frac{qE_{rad}(z,r,t)\cos(\alpha)}{m}\Delta t$$

$$v_y = v_{y_0} + \frac{qE_{rad}(z,r,t)\sin(\alpha)}{m}\Delta t$$

where z_0, x_0, y_0 and z, x, y are the position coordinates before and after Δt, $v_{z_0}, v_{x_0}, v_{y_0}$ and v_z, v_x, v_y are the velocities before and after Δt. E_{ax} and E_{rad} are the axial and radial electric field, as a function of axial and radial position and time (obtained from the argon ion - slow electron fluid model, see below), α is the azimuthal angle of the radial position (i.e. the angle of the radial position coordinates with respect to the x-axis), and q and m are the electron charge and mass, respectively.

The probability of collision during that time-step, $Prob_{coll}$, is calculated and compared with a random number between 0 and 1:

$$Prob_{coll} = 1 - \exp\left(-\Delta s \Sigma (n\sigma_{coll}(E))\right)$$

where Δs is the distance traveled during Δt; n and $\sigma_{coll}(E)$ are the densities of the target particles and the cross sections of the different collision types of the electrons with energy E. If the probability is lower than the random number, no collision occurs, and the Monte Carlo solver continues with the next electron during that time-step. If the probability is higher, a collision takes place. The collisions taken into account in the model, are elastic collisions with argon ground state atoms, electron impact ionization, excitation and de-excitation for all argon atom levels, copper atom and copper ion levels, as well as electron impact ionization from Ar^+ ions and two-electron impact ionization from Ar^0 to Ar^{2+}. Finally, also electron-electron Coulomb scattering is taken into account. To determine which collision takes place, the partial collision probabilities of the various collisions are calculated. The total collision probability, which is equal to one, because it is the sum over all partial collision probabilities, is subdivided in intervals with lengths corresponding to these partial collision probabilities. A second random number between 0 and 1 is generated, and the interval in which the random number falls, determines the collision that takes place. Then, the new energy and direction after collision are also defined by random numbers, based on energy and angular differential cross sections.

This procedure of calculating the trajectory by Newton's laws and treating the collisions by random numbers is repeated for the next electron during that time-step, and so on, until all electrons are followed. Then, the Monte Carlo procedure is repeated during the next time-step, again for all electrons, and so on, until a steady state is reached. However, the electrons can also be removed from the Monte Carlo model, when they undergo recombination at the cell walls, or (at least in the dc discharge) when they are transferred to the slow electron group. The latter occurs when they reach energies lower than the threshold for inelastic collisions. Indeed, these "slow" electrons are only important for carrying the electrical current and for providing negative space charge, and they can as well be described with a fluid model (see below), to save calculation time. However, when we want to calculate the detailed excitation and de-excitation between the various excited argon and copper levels for the collisional-radiative models (see below), all electrons, including the slow ones, are simulated with the Monte Carlo model, because low energy electrons can cause de-excitation or excitation to nearby levels. More information about this model can be found, e.g., in refs. [9-11].

2.3. Slow Electrons and Argon Ions: Fluid Model:

The slow electrons can be considered in thermal equilibrium with the electric field, and they are treated with a fluid model, together with the argon ions. As argon ionic species, Ar^+, Ar^{2+} and Ar_2^+ ions are taken into account in this model. The behavior of ions and electrons is described with continuity equations and transport equations based on diffusion and migration in the electric field. These equations are coupled to Poisson's equation to obtain a self-consistent electric field distribution, which is used in the electron and argon ion Monte Carlo models to calculate the trajectory by Newton's laws (see above and below). This yields the following equations:

$$\frac{\partial n_{Ar^+}(z,r,t)}{\partial t} + \overline{\nabla} \cdot \overline{j_{Ar^+}}(z,r,t) = R_{prod,Ar^+}(z,r,t) - R_{loss,Ar^+}(z,r,t)$$

$$\frac{\partial n_{Ar^{2+}}(z,r,t)}{\partial t} + \overline{\nabla} \cdot \overline{j_{Ar^{2+}}}(z,r,t) = R_{prod,Ar^{2+}}(z,r,t) - R_{loss,Ar^{2+}}(z,r,t)$$

$$\frac{\partial n_{Ar_2^+}(z,r,t)}{\partial t} + \overline{\nabla} \cdot \overline{j_{Ar_2^+}}(z,r,t) = R_{prod,Ar_2^+}(z,r,t) - R_{loss,Ar_2^+}(z,r,t)$$

$$\frac{\partial n_{e,slow}(z,r,t)}{\partial t} + \overline{\nabla} \cdot \overline{j_{e,slow}}(z,r,t) = R_{prod,e,slow}(z,r,t) - R_{loss,e,slow}(z,r,t)$$

$$\overline{j_{Ar^+}}(z,r,t) = \mu_{Ar^+} n_{Ar^+}(z,r,t)\overline{E}(z,r,t) - D_{Ar^+}\overline{\nabla} n_{Ar^+}(z,r,t)$$

$$\overline{j_{Ar^{2+}}}(z,r,t) = \mu_{Ar^{2+}} n_{Ar^{2+}}(z,r,t)\overline{E}(z,r,t) - D_{Ar^{2+}}\overline{\nabla} n_{Ar^{2+}}(z,r,t)$$

$$\overline{j_{Ar_2^+}}(z,r,t) = \mu_{Ar_2^+} n_{Ar_2^+}(z,r,t)\overline{E}(z,r,t) - D_{Ar_2^+}\overline{\nabla} n_{Ar_2^+}(z,r,t)$$

$$\overline{j_{e,slow}}(z,r,t) = -\mu_{e,slow} n_{e,slow}(z,r,t)\overline{E}(z,r,t) - D_{e,slow}\overline{\nabla} n_{e,slow}(z,r,t)$$

$$\nabla^2 V(z,r,t) + \frac{e}{\varepsilon_0}\left(n_{Ar^+}(z,r,t) + 2n_{Ar^{2+}}(z,r,t) + n_{Ar_2^+}(z,r,t) - n_{e,slow}(z,r,t) - n_{e,fast}(z,r,t)\right) = 0;\ \overline{E} = -\overline{\nabla} V$$

n and j, respectively, are the densities and fluxes of the argon ionic species and electrons, R_{prod} and R_{loss} are the production and loss rates. Production of Ar^+ ions is due to electron impact ionization, which is calculated in the electron Monte Carlo model above, as well as by Ar^{2+}-electron recombination. Loss of Ar^+ ions is due to Ar^+-electron recombination, atomic to molecular ion conversion from Ar^+ to Ar_2^+, and electron impact ionization from Ar^+ to Ar^{2+}. The production processes for the Ar^{2+} ions include electron impact ionization from Ar^0 and from Ar^+, as calculated in the Monte Carlo model above. The loss processes are Ar^{2+}-electron recombination and two-electron asymmetric charge transfer with Cu^0, being a resonant process [12]. Production of Ar_2^+ ions is caused by associative ionization of argon atoms (Hornbeck-Molnar process or due to the collision of two argon metastable atoms), as well as by atomic ion to molecular ion conversion (see above). Loss of Ar_2^+ ions is assumed to occur entirely due to dissociative recombination. Finally, production of the slow electrons is due to electron transfer to the slow electron group (calculated in the above electron Monte Carlo model), whereas loss of these electrons is due to various electron-argon ion recombination mechanisms. Further, $\overline{E}$ is the electric field and V is the electric potential. D and μ, respectively, are the diffusion coefficients and mobilities of the argon ionic species and electrons.

The four transport equations can be inserted into the four continuity equations. Together with Poisson's equation, this leads to a set of five coupled differential equations, with boundary conditions: $V=-V_c$ at the cathode (or $V(t)=V_{dc}+V_{rf}\sin(\omega_{rf}t)$ in the rf discharge; where V_{dc} is the dc bias voltage, V_{rf} is the applied rf voltage and ω_{rf} is the rf frequency) and $V=0$ at the anode; $n_{e,slow}=0$ at all walls and all times because electron-ion recombination at a conducting surface is assumed to be infinitely fast, and $\overline{\nabla} n_{Ar^+}$, $\overline{\nabla} n_{Ar^{2+}}$, $\overline{\nabla} n_{Ar_2^+} = 0$ at all walls and all times. The latter means that the ion fluxes at the walls are only due to migration. This forces a nonzero ion density at the electrodes, although it is expected that the ion density is zero or close to zero, due to Auger neutralization. Hence, this boundary condition is not completely correct, but it is used to avoid numerical difficulties due to a very thin ion diffusion boundary layer.

Due to the severe non-linearity and strong coupling of the equations, solving this model is a difficult numerical problem. The method we used was developed by Goedheer and coworkers [4], and is based on the Scharfetter-Gummel exponential scheme for the transport equations [13,14]. The basic idea is that the particle fluxes are assumed constant

between mesh points, instead of the densities. The advantage of this scheme is its ability to switch between situations where either the migration component or the diffusion component of the particle flux is dominant, namely in the high and low electric field, typical for the sheath region (cathode dark space; CDS) and bulk plasma (negative glow; NG), respectively. More details about this model can be found, e.g., in refs. [10,11,15].

2.4. Argon ions and Fast Argon Atoms in the CDS: Monte Carlo Model:

The argon ions are not really in equilibrium with the strong electric field in the CDS, and the fluid model is, therefore, only an approximation for the argon ions in this region. Therefore, the argon ions are also simulated with a Monte Carlo method in this region, which enables us to calculate the argon ion energy distribution at the cathode, needed to calculate the amount of sputtering (see below). Only the Ar^+ ions are treated with this Monte Carlo model, because the Ar^{2+} and Ar_2^+ ions have a lower density and flux, and they play only a minor role in the sputtering process [15]. However, beside the Ar^+ ions, also fast (i.e., non-thermal) argon atoms (Ar^0_f), which are created by collisions of the argon ions, are described with this Monte Carlo model, since it was found that they play a dominant role in the sputtering process [9].

The argon ion and fast argon atom Monte Carlo model is similar to the electron Monte Carlo model. During successive time-steps, the trajectory of a large number of ions and atoms is calculated by Newton's laws, and the occurrence of a collision, the nature of the collision and the new energy and direction after collision are determined by random numbers. The collision processes taken into account are elastic scattering collisions with argon ground state atoms, for both ions and atoms, symmetric charge transfer for argon ions (which is actually also a form of elastic collisions, because there is no change in kinetic energy), and ion and atom impact ionization, excitation and de-excitation for all argon atom levels. More information about this Monte Carlo model can be found in refs. [9,16,17].

2.5. Argon Atoms in Excited Levels: Collisional-Radiative Model:

The argon atoms in various excited levels are described with a so-called collisional-radiative model. This is actually a kind of fluid model, which consists of a set of balance equations (one for each excited level) with different production and loss terms. The name "collisional-radiative" model stems from the fact that the production and loss processes are typically due to collisions or radiative decay (see below).

Figure 1 shows a schematic energy diagram of the argon atomic levels taken into account in our model. 64 argon atomic excited levels are considered; most of them are effective levels, i.e., a group of individual levels with comparable excitation energy and quantum numbers. The four 4s levels, of which two are metastable and two are resonant levels, are however treated separately, because they have a longer lifetime and they play

an important role in the glow discharge (see below). The behavior of these levels is described with 64 coupled balance equations, taking into account a large number of populating and depopulating collisional and radiative processes:

$$\frac{\partial n_{Ar^*}(z,r,t)}{\partial t} - D_{Ar^*}\frac{1}{r}\frac{\partial}{\partial r}\left(r\frac{\partial n_{Ar^*}(z,r,t)}{\partial r}\right) - D_{Ar^*}\frac{\partial^2 n_{Ar^*}(z,r,t)}{\partial z^2} = R_{prod}(z,r,t) - R_{loss}(z,r,t)$$

The production and loss processes taken into account are: electron, argon ion and atom impact ionization from all levels, excitation and de-excitation between all these levels, and electron-ion three-body and radiative recombination to all levels, as well as radiative decay between the levels and Hornbeck-Molnar associative ionization (for Ar* levels with excitation energy above 14.7 eV). Moreover, some additional processes are incorporated for the 4s metastable levels, namely metastable atom - metastable atom collisions, Penning ionization of the sputtered copper atoms, and two-body and three-body collisions with argon ground state atoms.

Transport of the 4s metastable levels occurs by diffusion. When the two resonant 4s levels decay to the ground state, a large fraction of the emitted radiation is re-absorbed by the ground level, leading again to formation of these 4s levels. This phenomenon of "radiation trapping" is accounted for by means of "escape factors" which express the fraction of photons which can really escape without being re-absorbed [18,19].

The 64 balance equations are coupled to each other, because higher and lower levels affect each other due to radiative decay, excitation and deexcitation. The boundary conditions for these equations are $n_{Ar^*}=0$ at all walls, because the excited levels will de-excite upon collision at the walls. More information about this model can be found in ref. [20].

2.6. Sputtering at the Cathode: Empirical Formula:

The flux of sputtered copper atoms at the cathode is calculated from the flux energy distribution functions of the argon ions, fast argon atoms and copper ions (see below) bombarding the cathode, f(0,r,t,E), calculated in the Monte Carlo models, multiplied with an empirical formula for the sputtering yield as a function of the bombarding energy (Y), adopted from ref. 21:

$$J_{sput}(0,r,t) = -\int_E \left\{Y_{Ar-Cu}(E)\left[f_{Ar^+}(0,r,t,E) + f_{Ar_f^0}(0,r,t,E)\right] + Y_{Cu-Cu}(E) f_{Cu^+}(0,r,t,E)\right\} dE$$

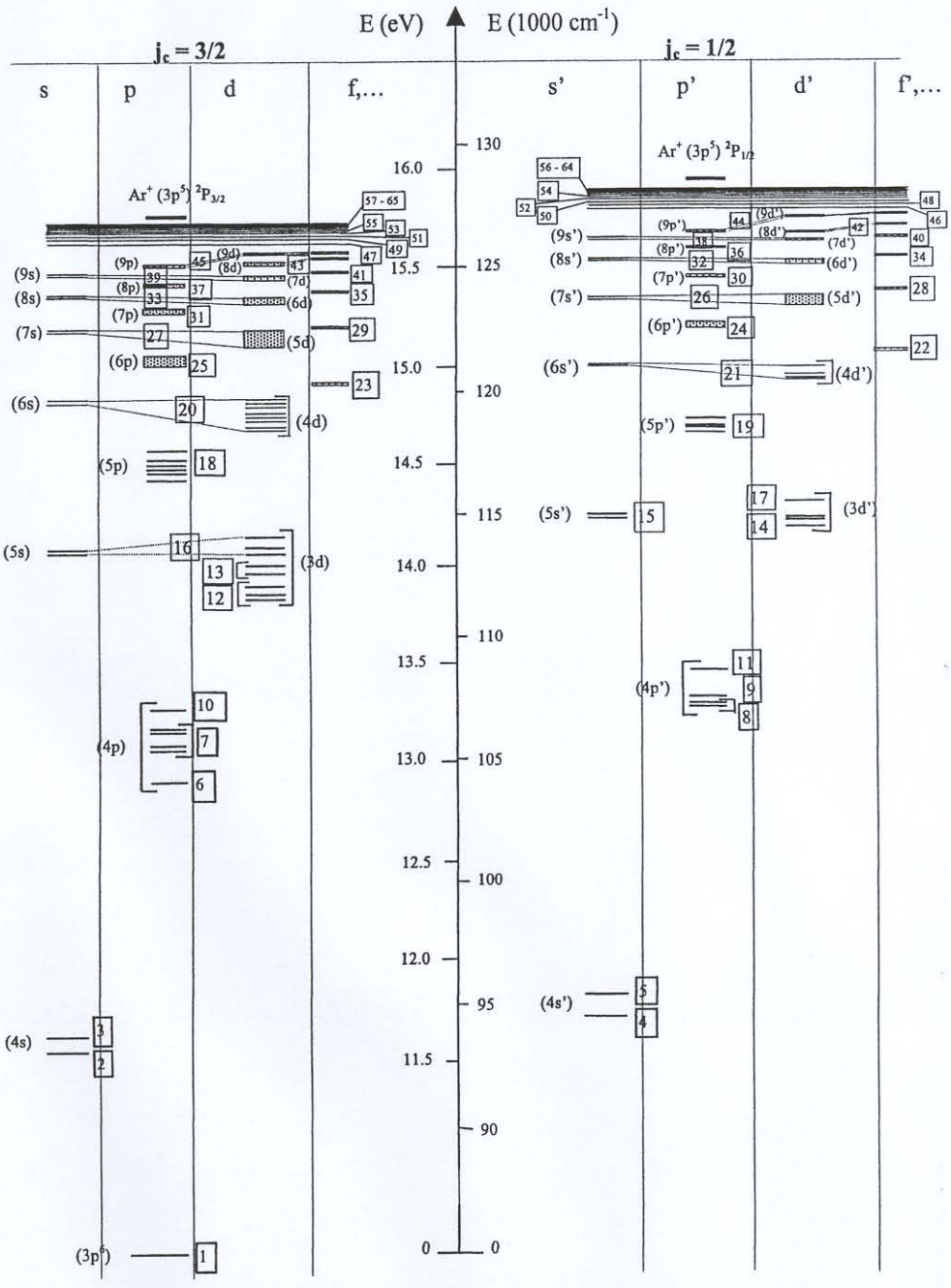

Figure 1: Argon atom energy level scheme, illustrating all the effective levels incorporated in the model. Reproduced from ref. 20 by permission of the American Institute of Physics.

2.7. Thermalization of the Sputtered Copper Atoms: Monte Carlo Model:

When the copper atoms are sputtered from the cathode, they have energies in the order of several eV. However, they lose these energies almost immediately in the first mm's from the cathode, by collisions with argon gas atoms, until they are thermalized. This thermalization process is described with a Monte Carlo model, similar to the electron Monte Carlo model (see above), except that the electric field does not come into play for the neutral atoms, and that only elastic collisions with argon atoms are incorporated. Indeed, collisions with other plasma species can be neglected, due to the lower densities of these species. This Monte Carlo model is run until all atoms are thermalized, and it results in a so-called thermalization profile, F_T, i.e., the number of atoms thermalized as a function of position from the cathode. More details can be found in ref. 22.

The product of J_{sput} and F_T will be used as source term for the copper atoms, described in the next model.

2.8. Further Behavior of the Copper Atoms and Ions: Collisional-Radiative Model:

The further behavior of the thermalized sputtered copper atoms (i.e., transport, ionization and excitation), and the behavior of the excited copper atoms and of the copper ions, both in the ground state and in excited levels, is described with a collisional-radiative model. Eight copper atom levels, seven copper ion (Cu^+) levels and the Cu^{2+} ions are considered (see the energy level scheme in figure 2). Some of the Cu atom and ion levels are grouped into effective levels. The behavior of all the levels is again described with a set of coupled balance equations with various production and loss terms, i.e., electron impact ionization from all levels, excitation and deexcitation between all levels, radiative decay between all levels, electron-ion three-body recombination to the upper copper atom and copper ion levels, Penning ionization by argon metastable atoms, and asymmetric charge transfer between copper atoms and argon ions. Moreover, an additional production term for the copper ground state atoms is the product of J_{sput} and F_T, as is described above.

Transport of the copper atom ground state and metastable levels occurs by diffusion, whereas diffusion and migration govern the transport of the copper ion ground state and metastable levels. The 16 equations are coupled due to the effect of higher and lower levels on the other levels, and they are solved until steady state is reached. More information about this model is given in ref. 23.

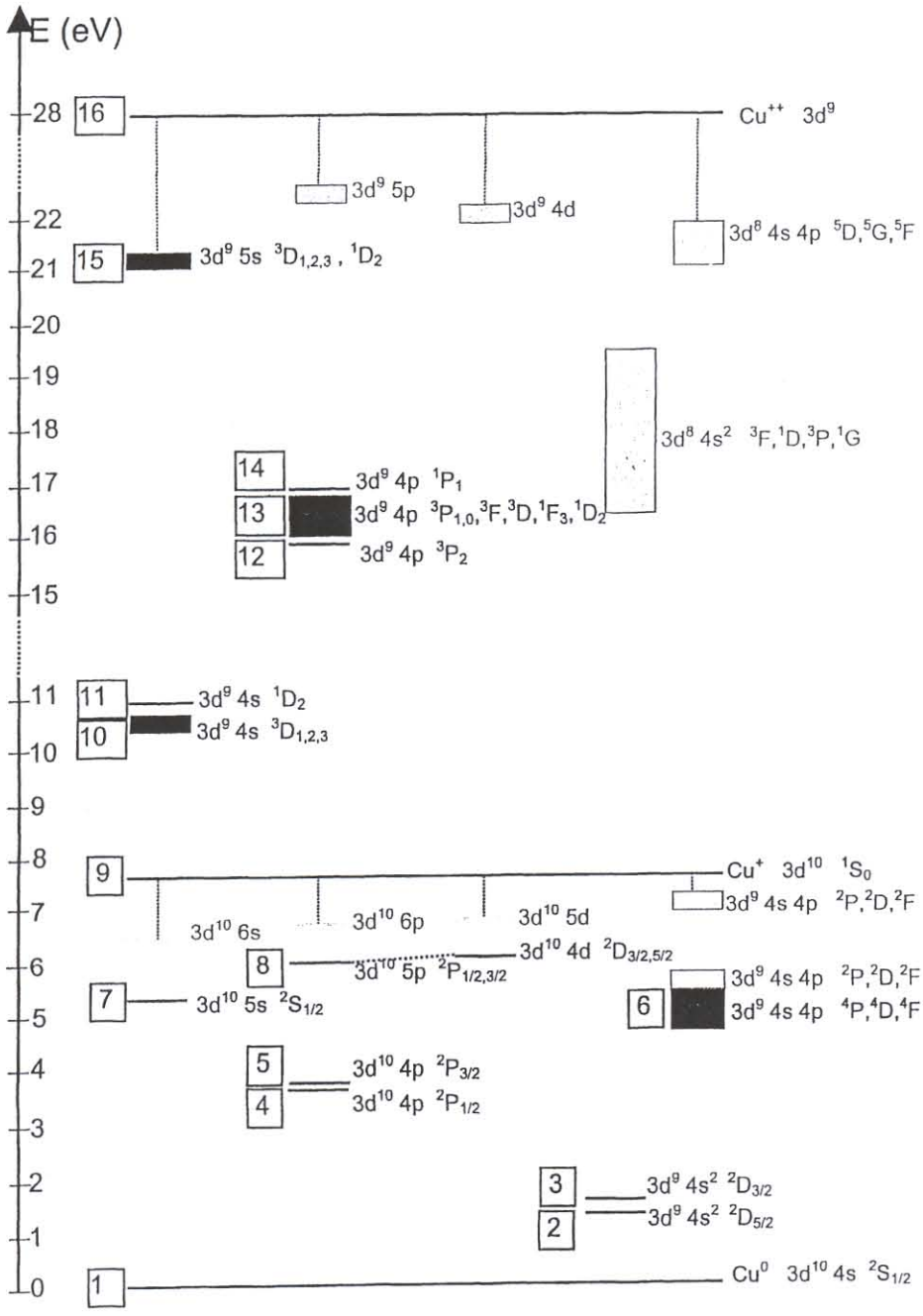

Figure 2: Copper atom and ion energy level scheme, with the effective level number (left) and the designation according to Moore (right of the levels). The levels considered in the model are presented in black. Reproduced from ref. 23 by permission of Elsevier Science Inc.

2.9. Copper Ions in the CDS: Monte Carlo Model:

The copper ions are also treated with a Monte Carlo model in the CDS, because they are not in equilibrium with the strong electric field in this region. The procedure is again comparable to the electron Monte Carlo model; it includes calculation of the trajectory by Newton's laws, and treatment of the collisions by random numbers (for more information, see e.g., ref. 24.

2.10. Coupling of the Models:

All the above models are coupled to each other due to the interaction processes between the species, i.e., the output of one model is used as input for the next model, and so on. The models are solved iteratively until final convergence is reached, to obtain an overall picture of the glow discharge. The entire calculation procedure takes several days to more than a week on a professional workstation.

3. Illustration of Some Typical Calculation Results

The modeling network has been applied mainly to dc glow discharges, although capacitively coupled rf discharges and microsecond pulsed discharges have also been described. An overview of the typical quantities that have been calculated with the models, is given in Table 2. Comparison with experimental data is made, when available. In the following, some of the calculation results will be discussed in more detail, to illustrate the possibilities and limitations of the models.

3.1. Electrical Characteristics and Electrical Operation Modes:

The input parameters in the model are the cell geometry, the kind of discharge gas and the corresponding cross sections, as well as the discharge voltage, the gas pressure and temperature. The electrical current follows normally self-consistently from the calculation results, as the sum of the microscopic fluxes of the charged plasma species. In order to obtain good agreement between the calculated current and the experimental value, we slightly adapt the gas temperature, because the latter parameter is generally unknown, and it greatly affects the calculation results. However, care is taken that the assumed gas temperature values are always in a realistic range, as found by experiments and as calculated with our heat transfer model.

In the dc glow discharge, current and voltage are constant in time, and this applies also to all other calculation results, as soon as steady-state is reached. This is not the case in the rf and pulsed operation mode, where current and voltage, and hence all other calculation results, vary as a function of time. Therefore, it is essential to calculate the

correct time-behavior of the electrical characteristics, before reliable calculation results can be expected for the other plasma quantities.

Figure 3 presents the calculated voltage (a), electrical current (b) and power (c) as a function of time in one rf-cycle, at typical analytical rf-GD-OES conditions (i.e., a pressure of 850 Pa, an rf voltage with amplitude of 403 V, a peak-to-peak current of about 150 mA and a power of 6.5 W, in a cell with typical dimensions of 4 mm diameter and 1.5 cm length. The rf-electrode is located at the left (with a diameter of 4 mm) and the other cell walls are grounded. Hence, the size of the rf-electrode is much smaller than that of the grounded electrode. The corresponding experimental data, at exactly the same conditions and in a commercial GD-OES cell, are illustrated with the dashed lines. The voltage at the rf-electrode is characterized by a sinusoidal profile, both in the theoretical and the experimental results:

$$V(t) = V_{rf} \sin(\omega t) + V_{dc-bias}$$

where V_{rf} and $V_{dc\text{-}bias}$ are the rf-amplitude and the dc-bias voltage, respectively, and ω is the rf-frequency. Only ω and V_{rf} are used as input in the model, in addition to the gas pressure and temperature. $V_{dc\text{-}bias}$ is calculated in the model, based on the condition that the ion and electron currents to the rf-electrode, integrated over one rf-cycle, should be equal to each other. When the electron current was calculated to be higher, the dc-bias was made more negative in the model, to attract more ions and to repel the electrons; and vice versa. The calculated and measured dc-bias values are illustrated with the thin solid and dashed lines, respectively. It appears that excellent agreement is reached between the calculated and measured values of $V_{dc\text{-}bias}$. Because of this large negative dc-bias, the voltage at the rf-electrode is negative during most of the rf-cycle, both in the calculated and in the measured results; it is only slightly positive around $\omega t=\pi/2$.

The calculated and measured electrical currents at the rf-electrode are illustrated in figure 3b with solid and dashed lines, respectively. The agreement is not perfect, i.e., experimentally an almost perfect sinusoidal profile with a superimposed positive peak around $\omega t=\pi/2$ is obtained, which is not exactly found back in the calculated results. However, apart from this fine-structure in the time-profile, the agreement is very reasonable. The current is highly positive around $\omega t=\pi/2$, which is due to a large electron flux bombarding the rf-electrode. In the rest of the rf-cycle, the current is negative and mainly attributed to ions bombarding the rf-electrode. The displacement current, which results from expansion and contraction of the rf-sheath, is found to be not so important at typical analytical rf-GD-OES conditions (it was at maximum found to be equal to the ion current). This results again from the large negative dc-bias, which makes the analytical rf glow discharge look similar to a dc glow discharge. Hence, the thickness of the rf-sheath does not change much with time, and consequently the displacement current is rather low. It appears that voltage and current are roughly in phase with each other, at these typical conditions, both in the calculation results and in the experimental data. The corresponding electrical power as a function of time, which is simply calculated as the product of voltage and current, is presented in figure 3b (solid and dashed lines for the

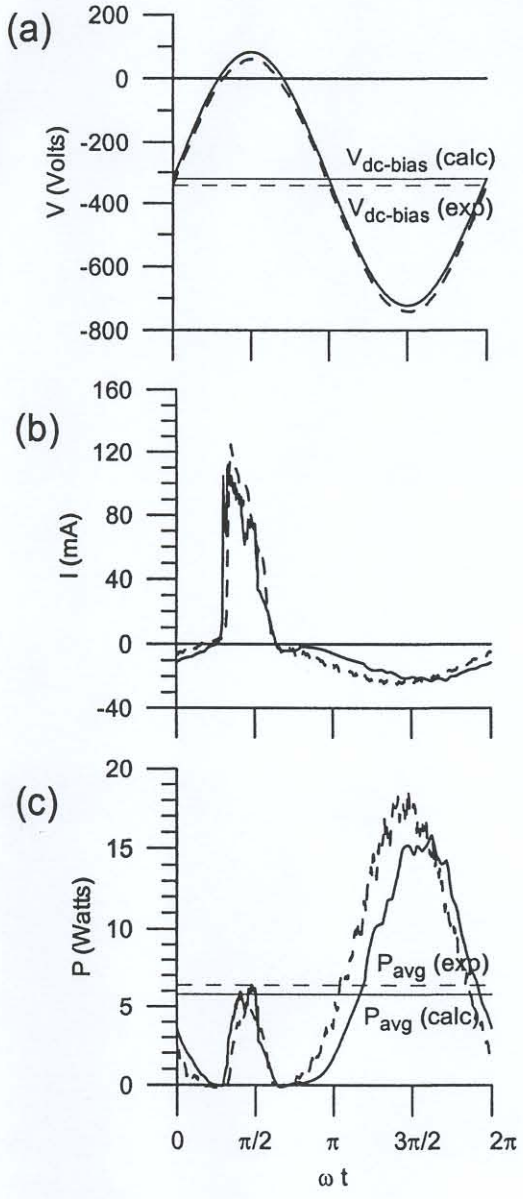

Figure 3: Calculated (solid lines) and measured (dashed lines) electrical characteristics as a function of time in the rf-cycle, in an argon rf glow discharge at a gas pressure of 850 Pa, an rf voltage with amplitude of 403 V, an electrical power of 6.5 W, and cell dimensions of 4 mm diameter and 1.5 cm length. (a) voltage (the calculated and measured dc-bias voltages are presented by the thin solid and dashed lines, respectively); (b) current; (c) power (the calculated and experimental average power values are indicated with the thin solid and dashed lines, respectively).

calculated and measured results, respectively). The time-averaged calculated and measured values are illustrated with thin solid and dashed lines, respectively. The agreement is not perfect, but it is very reasonable. Consequently, the calculated and measured averaged values are also in satisfactory agreement with each other.

For the rf glow discharge, reasonable agreement between calculated and experimental data could be reached for the voltage, current and power as a function of time, when assuming a constant gas temperature. This appeared not to be the case for the pulsed discharge. Indeed, it was found that when the gas temperature was assumed constant in time, the model could not predict the experimental electrical current and power behavior as a function of time in a microsecond (μs) pulsed glow discharge. Therefore, we had to adjust the gas temperature as a function of time during and after the pulse, in order to obtain reasonable agreement between calculated and measured electrical current and power as a function of time.

Figure 4 shows the applied voltage (the experimental value is used as input in the model) (a), the calculated and measured electrical current (b) and power (c) (calculated and measured values represented by solid and dashed lines, respectively), as well as the assumed gas temperature (d), all as a function of time during and after the pulse. The gas pressure was measured to be 400 Pa and assumed constant in time. A voltage of 1500-2000 V is applied during 10 μs, and then it drops exponentially, reaching zero at about 40 μs after initiation of the pulse (see figure 4a). The electrical current (figure 4b), and hence also the power (figure 4c), appear to rise significantly to values of almost 1 A and 1.5 kW, respectively, at 1.5-2 μs, and then they drop almost as rapidly to "plateau values" of about 100 mA and 200 W, respectively, which are more or less maintained from 4 to 10 μs. After the pulse, the current and power decay to zero at about 20 μs after the start of the pulse. This experimental behavior of current and power could only be predicted with our model if the gas temperature was assumed to vary in time, as illustrated in figure 4d. Indeed, at the start of the pulse, the gas is at room temperature. However, the gas temperature will increase rapidly as a function of time, due to the high electrical power, and hence high power input into the argon gas. When the power has dropped to a plateau value of ca. 200 W, the gas temperature will not further increase, but on the other hand, the power is still high enough to maintain the high gas temperature. Only when the power has dropped further, after the pulse, the gas temperature decreases exponentially. It was found to reach room temperature again around 200 μs [25], hence well before the next pulse will be applied, at the pulse repetition frequency of 200 Hz used in the experiment. The time-evolution of the gas temperature presented in figure 4d was used as a kind of fitting parameter in our model, to obtain reasonable agreement with the experimental behavior of voltage, current and power as a function of time. Nevertheless, the assumed values have also been checked, at least qualitatively, with a time-dependent heat transfer equation, and it was illustrated that the fitted time-evolution of the gas temperature was indeed realistic [28].

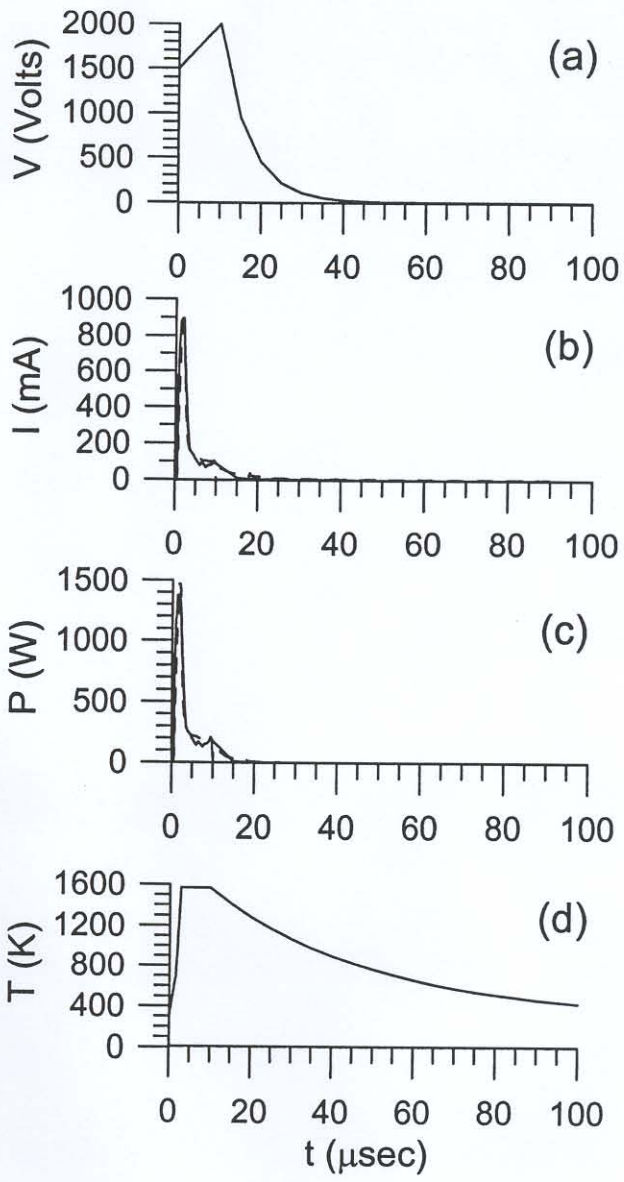

Figure 4: Calculated (solid lines) and measured (dashed lines) electrical characteristics as a function of time during and after the pulse, in a μs-pulsed argon glow discharge at a gas pressure of 400 Pa, an applied voltage of 2 kV, a pulse width of 10 μs and a pulse repetition frequency of 200 Hz. Only the pulse period and a fraction of the afterglow are illustrated. (a) voltage (the experimental voltage time-profile is used as input in the model); (b) calculated and measured current; (c) calculated and measured electrical power; (d) gas temperature assumed in the model.

Because the analytical rf glow discharge greatly resembles a dc glow discharge (see electrical characteristics above), and the µs-pulsed glow discharge behaves also as a short dc glow discharge followed by a long afterglow, most of the calculated plasma quantities (see Table 2) are very similar in the dc, rf and µs-pulsed operation modes. Therefore, in the following, we will focus on the calculation results for the dc glow discharge, which have already been more thoroughly validated in the past few years.

Table 2: Overview of the typical results obtained with our models, and comparison with experimental data, if available.

Calculated quantities	Comparison with experimental data (if available)
Electrical characteristics:	
dc: current as a function of voltage and pressure	measured in a range of different conditions
rf: voltage, current and power as a function of time in the rf-cycle	measured in a range of different conditions
µs-pulsed: voltage, current and power as a function of time during and after the pulse	measured for one condition
Potential, electric field distributions:	
2D potential distributions	-
2D axial and radial electric field distributions	-
Value of the plasma potential	-
Lengths of the different regions (CDS, NG)	Length of CDS as function of pressure and current: in agreement with empirical formula of Aston [25]
3D density profiles of:	
* argon atoms (gas heating)	-
* argon ions	-
* fast argon atoms	-
* argon metastable atoms	measured (for dc glow discharge) by laser induced fluorescence (LIF)
* other argon excited levels	-
* fast electrons	-
* thermalized electrons	measured by Langmuir probe (dc glow discharge)
* atoms of the cathode material	measured by LIF (dc glow discharge)
* ions of the cathode material	measured by LIF (dc glow discharge)
* atoms + ions of the cathode material, in excited levels	
Ion fluxes of argon and cathode ions at the exit slit of the cell to the glow discharge mass spectrometer (dc).	ratio in qualitative agreement with ratios in dc GDMS mass spectra
Ionization degrees of argon and cathode atoms	based on the LIF results (see above)
3D energy distributions and mean energies of:	
* electrons	-
* argon ions	measured at cathode for dc glow discharge
* fast argon atoms	-
* cathode ions	measured at cathode for dc glow discharge
Information about collision processes:	
* 3D collision rates of the different collision processes of electrons, argon ions and fast argon atoms, and relative importances of these collision processes	-
* 3D rates of Penning ionization, asymmetric charge transfer and electron impact ionization, and relative contributions to the total ionization of sputtered atoms	-
* 3D rates and relative contributions of the various populating and depopulating processes (see text) of the metastable and other excited argon levels	-
* 3D rates and relative contributions of the various populating and depopulating processes (see text) of the excited cathode atom + ion levels	

Information about sputtering: * Sputtering (erosion) rates at the cathode * Thermalization profiles of the sputtered atoms * Amount of redeposition on the cathode by backscattering or backdiffusion * Relative contributions of argon ions, fast argon atoms and cathode ions to the sputtering process * 2D crater profiles due to sputtering at the cathode	 values measured in a range of different conditions, in a dc, rf and μs-pulsed glow discharge - - - profiles obtained for a dc glow discharge cell
Emission spectra and emission spatial distributions due to radiative decay from the excited levels (for argon and cathode atoms + ions)	optical emission spectra from the literature [26] emission intensities for some specific lines as a function of distance from the cathode (dc glow discharge) emission intensities for some specific lines as a function of discharge conditions (dc glow discharge)
Effect of cell geometry on the calculated quantities	-
Prediction of variations in relative sensitivity factors for GDMS	data from the literature [27]

3.2. Potential and Electric Field Distributions:

Figure 5 illustrates the calculated two-dimensional potential distribution, for dc glow discharge conditions of 440 Pa, 800 V and 8.7 mA. The cathode is found at the left of the figure (with a diameter of 4 mm), whereas the other cell walls are at anode potential (grounded). The potential is equal to –800 V at the cathode, and increases very rapidly towards zero at about 0.4-0.5 mm from the cathode. This position where the potential crosses zero is defined in our model as the interface between cathode dark space (CDS) and negative glow (NG). In the NG, the potential is slightly positive (approximately 10 V for these discharge conditions and cell geometry). This value is called the "plasma potential". It drops again to zero at the anode walls, which are grounded. The electric field distribution can easily be derived from the potential distribution, by taking the spatial gradient. This leads to a strongly negative electric field in the CDS, which is responsible for the significant energy gain of electrons and ions in this region. In the NG, a weak electric field, both positive and negative, depending on the position, is found.

3.3. Densities and Level Populations of the Plasma Species:

Figure 6 presents the two-dimensional Ar^+ ion density profile, calculated for the same conditions as in figure 5. The density is rather low and constant in the CDS, but it increases rapidly in the NG, and reaches a maximum of about $2x10^{13}$ cm^{-3} at 1-1.5 mm from the cathode. The density increases again to low values at the anode walls. The density profile of the electrons (not shown here) is characterized by nearly the same profile as the Ar^+ ion density profile, except that it is almost zero in the CDS. This gives rise to a positive space charge in the CDS and nearly charge neutrality in the NG, which results in the typical potential distribution shown in figure 5.

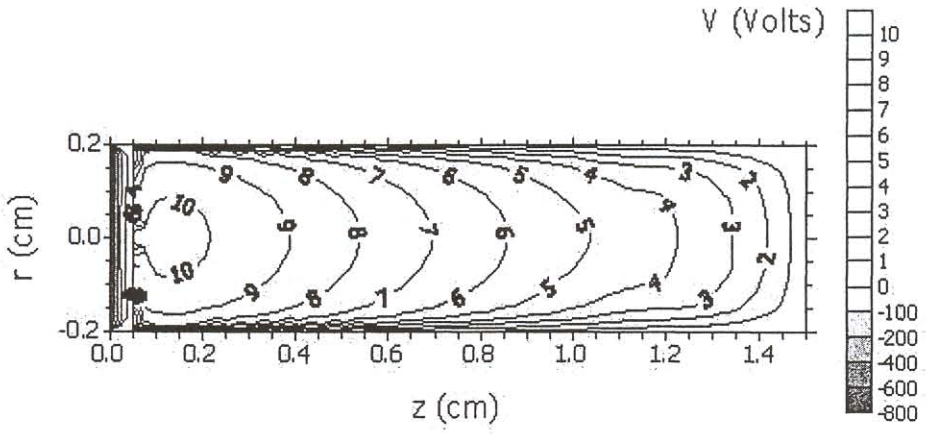

Figure 5: Calculated two-dimensional potential distribution in a dc argon glow discharge, at a pressure of 440 Pa, a voltage of 800 V, and an electrical current of 8.7 mA. The cathode is found at the left end of the figure, whereas the other boundaries represent the grounded anode walls of the glow discharge cell.

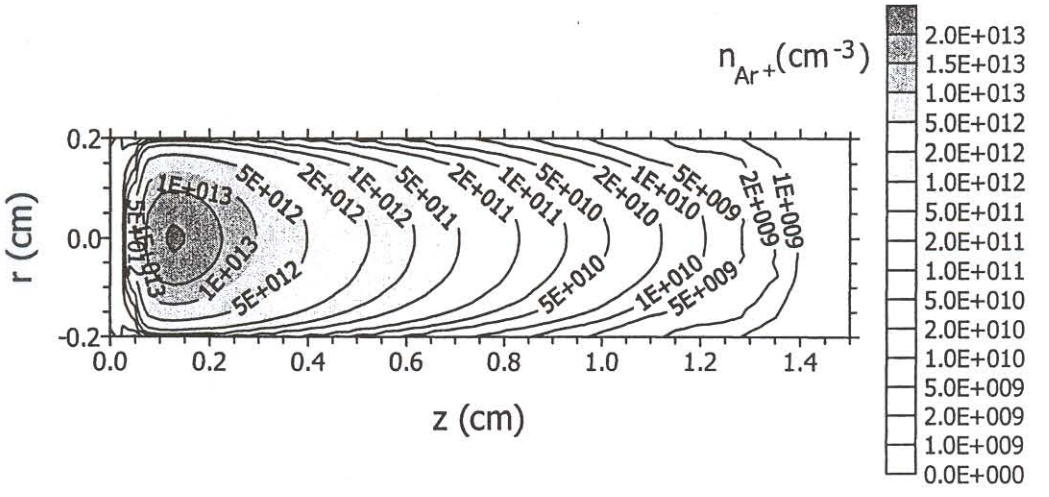

Figure 6: Calculated two-dimensional density profile of the argon ions in a dc glow discharge, at the same operating conditions as in figure 5.

To check our calculation results for the electron densities, we have performed Langmuir probe measurements in a similar (Grimm-type) glow discharge geometry, for a range of different pressures and voltages [29]. Figure 7 shows the calculated electron densities at the maximum of their profile (solid lines, left axis) [30], as well as the measured results (dashed lines, right axis). The results are in satisfactory agreement, insofar that both calculated and experimental values rise to nearly the same extent with voltage and pressure. Quantitatively, we found a factor of about 2 difference (note the different scales in the y-axes). This is, however, still reasonable because it is well below the expected errors of both the model calculations (e.g., uncertainties in input data, like gas pressure and temperature and collision cross sections, of which small variations can yield significant variations in the calculation results) and the experimental data (e.g, possible disturbance of the plasma by the Langmuir probe, possible contamination due to deposition on this probe, approximations in the Langmuir probe theory).

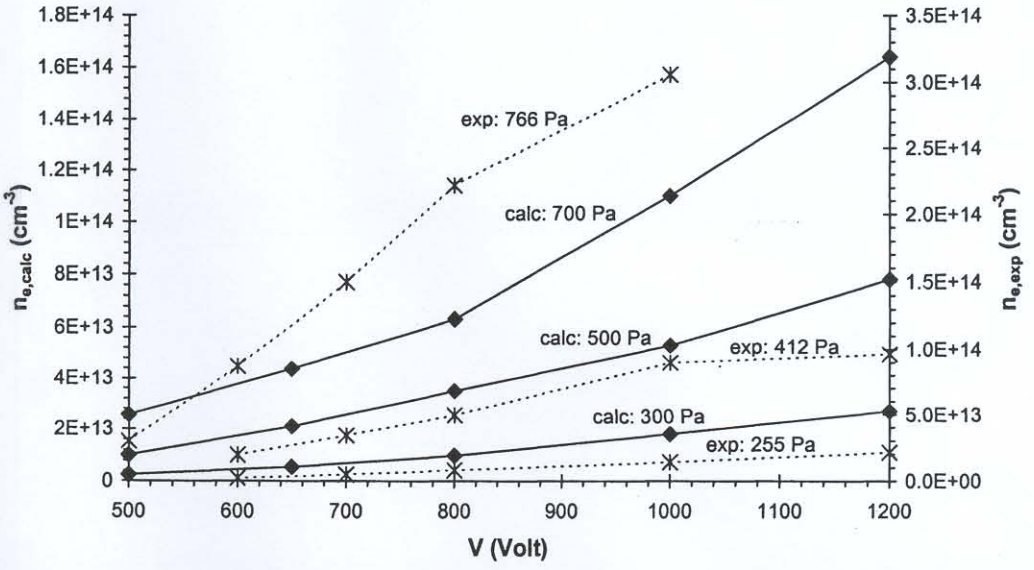

Figure 7: Calculated (solid lines, left axis) and measured (with a Langmuir probe, dashed lines, right axis) electron number densities in a dc glow discharge, as a function of voltage at different pressures. Reproduced from ref. 30 by permission of Elsevier Science Inc.

In Figure 8, the calculated level populations of the argon atoms in excited levels, at the maximum of their profiles, are illustrated, as a function of their excitation energy, for the same conditions as in figures 5 and 6. For comparison, the ground state atom density is about 6.5×10^{16} cm^{-3} at the pressure of 440 Pa and a gas temperature of about 500 K. Hence, this is at least 3-4 orders of magnitude higher than the excited level populations. Since most of the excited levels were grouped together into effective levels (see Figure 1 above) with hence a much larger statistical weight, we have divided the level populations

by the corresponding statistical weights, to exclude this effect. It is clear that the level populations of the 4s metastable and resonant levels are much higher (at least two orders of magnitude) than the populations of the higher excited levels. This is logical because the metastable levels cannot decay to the ground state by emission of radiation. The resonant levels can decay, but a large fraction of the emitted radiation (in the order of 99.99%) will be reabsorbed by the ground state (i.e., so-called radiation trapping; see above), so that the resonant levels have also rather high population densities. The populations of the higher levels drop rapidly with increasing excitation energy. The curve of log(density) vs. excitation energy (Boltzmann plot) is not a straight line. Hence, the excited argon levels are not Boltzmann distributed at the conditions under study, which is like expected because the analytical glow discharge is far from LTE.

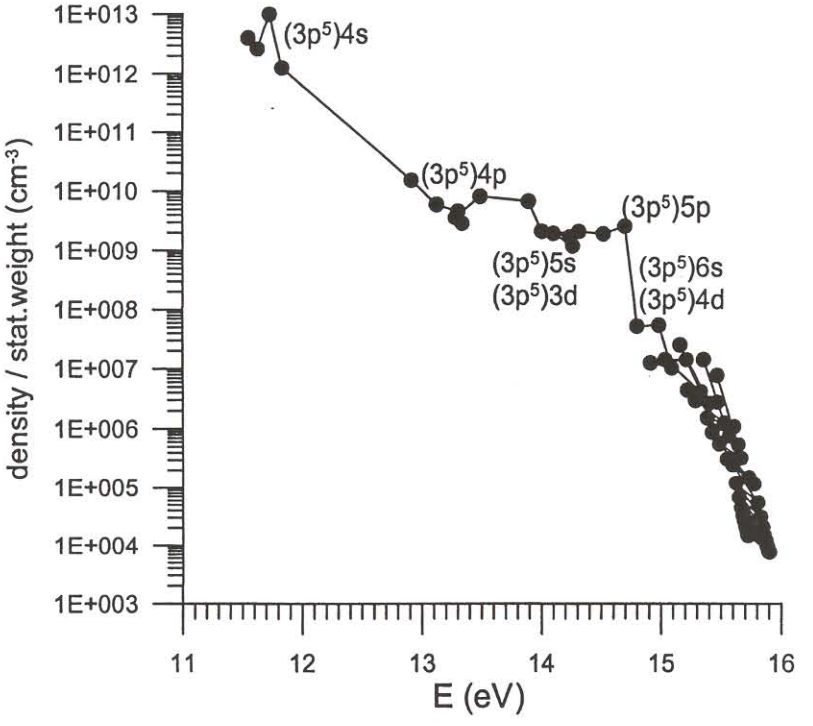

Figure 8: Calculated level populations at the maximum of their profiles, divided by the statistical weights of the levels, for various argon atomic excited levels, as a function of their excitation energy, in a dc glow discharge, at the same conditions as in figure 5.

The level populations of the copper atoms and ions in the ground state and in excited levels, at the maximum of their profile, are plotted as a function of excitation energy in Figure 9, for the same conditions as in figures 5, 6 and 8. Again, the level populations are divided by the statistical weight, to exclude the effect of effective levels with larger statistical weight. The ground state densities of both copper atoms and ions (i.e., about 10^{14} cm^{-3} and $6.5x10^{11}$ cm^{-3}, respectively) are clearly higher than the excited level populations, and the latter generally decrease with excitation energy. It appears that the Cu^+ $3d^9$ 4p $^3P_2$ level is exceptionally high compared to the other $3d^9$ 4p levels. The reason is that this level can be selectively excited by asymmetric charge transfer with argon ions, due to good energy overlap [23]. The latter is also experimentally demonstrated, since the lines originating from this level are extremely high in comparison with other emission lines [31], which validates our calculation results.

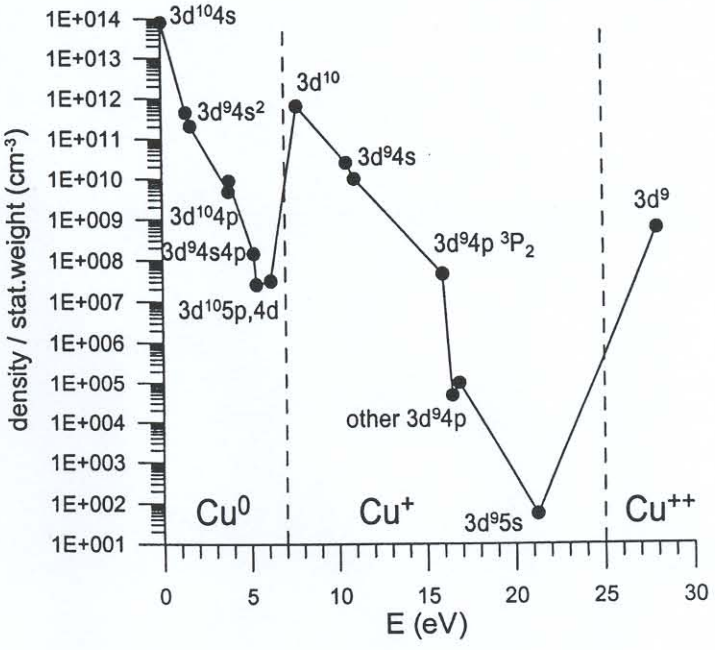

Figure 9: Calculated level populations at the maximum of their profiles, divided by the statistical weights of the levels, for various Cu^0 and Cu^+ excited levels, as well as for the Cu^{++} ions, as a function of their excitation energy, in a dc glow discharge, at the same conditions as in figure 5.

At this point it is worthwhile to mention that we have also measured two-dimensional density profiles of argon metastable atoms, and of sputtered tantalum atoms and ions, by laser-induced fluorescence spectrometry. When our model (this time for tantalum instead of copper, because of the availability of suitable laser lines) was applied to the experimental conditions, the results were in fairly good agreement, as is illustrated in refs [32,33].

3.4. Energies of the Plasma Species:

In the Monte Carlo models, the energies of the plasma species are explicitly calculated, without making any assumptions. Figure 10 presents the calculated flux energy distribution of the electrons, as a function of distance from the cathode, in a dc glow discharge at 1000 V, 75 Pa and 3.5 mA [34]. The electrons leave the cathode (z=0, not indicated in the figure) with low energy (assumed to be 4 eV on the average [35]), but they gain energy from the electric field as they move in the CDS towards the NG. At the same time, however, they lose energy due to collisions, so that their energy distribution spreads out from zero toward the maximum energy, with all energy values being more or less of equal probability. At the CDS-NG interface, which is located at 0.24 cm from the cathode at these conditions, the maximum energy is equal to the total discharge voltage of 1000 V. In the NG, however, the electrons do not gain much energy anymore from the weak electric field, but they lose their energy very efficiently due to collisions. Hence, the energy distribution shifts towards lower energies. Nevertheless, even at the end of the discharge cell, there is still a small peak at maximum energy, which indicates that there are still some electrons which have traversed the entire discharge without collisions, at the discharge conditions under investigation.

In contrast to the electron flux energy distribution, the energy distribution of the argon ions is not characterized by a peak at maximum energy. This is clearly shown in figure 11a, which shows the calculated flux energy distribution of the argon ions as a function of distance from the cathode in the CDS, at the same discharge conditions as in figure 10 [34]. The argon ions are assumed to have thermal energies in the NG, but when they enter the CDS, they gain energy from the electric field. However, they also lose energy due to collisions. It appears that the collisions of the ions (mainly elastic scattering) are more frequent and more efficient for losing energy than the collisions of the electrons (mainly ionization and excitation), because most argon ions have rather low energies when they arrive at the cathode (z=0 cm).

The energy distribution of the argon ions bombarding the cathode has been measured in a similar cell and for similar conditions as used in the calculations [36]. The results are shown in figure 11b. A dip was obtained at low energy as well as a peak at negative energy, which were probably the results of experimental artifacts. Indeed, it was suggested that low energy ions were subject to charge transfer collisions (for which the cross section is, indeed, larger at low energies) immediately outside the discharge cell, in the acceleration region of the mass spectrometer. This gives rise to some loss for low

energy ions, explaining the dip, because the ions disappear from the energy distribution, as well as some production (i.e., a peak) at negative energy, because these ions have not attained the maximum acceleration voltage. Therefore, the expected "real" energy distribution is indicated by the dashed line in figure 11b, and the latter agrees qualitatively with the calculated results.

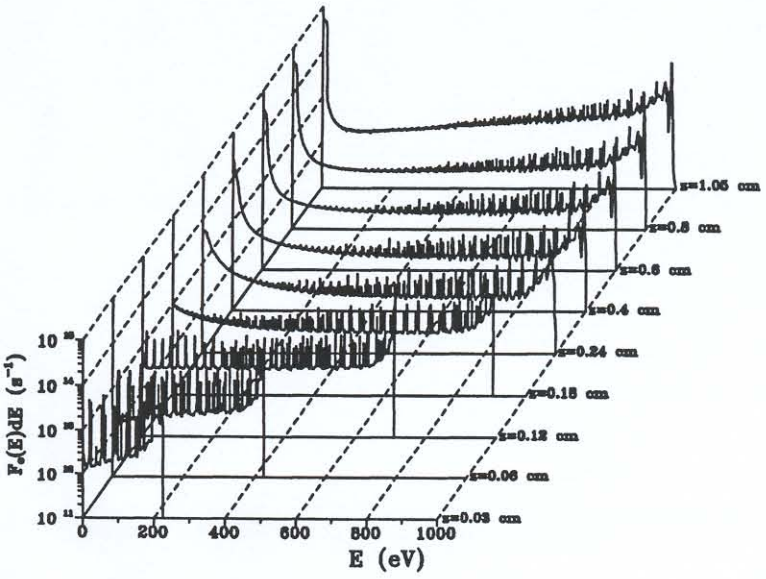

Figure 10: Calculated flux energy distribution of the electrons, as a function of distance from the cathode, in a dc argon glow discharge, at a pressure of 75 Pa Torr, a voltage of 1000 V and a current of 3.5 mA. Reproduced from ref. 34 with permission of the Royal Society of Chemistry.

Fairly good qualitative agreement was also reached between the calculated and measured energy distributions of the copper ions bombarding the cathode. Figure 12a shows the calculated energy distribution of the copper ion flux in the CDS, at various positions from the cathode, for the same discharge conditions as in figure 11 [34]. The copper ions have also thermal energy in the NG, where most of them were formed, but when they diffuse into the CDS, they gain energy from the electric field and are accelerated towards the cathode. In contrast to the argon ions, they do not lose their energy very efficiently in collisions. Hence, they are characterized by a pronounced peak at maximum energy (note the logarithmic scale). The same pronounced peak is also experimentally observed, as appears from figure 12b [36]. Three estimated pressure values are indicated for the three experimental energy distributions, because the pressure could actually not be measured inside the glow discharge cell during the experiments. Exact quantitative comparison can, therefore, not be carried out, but the qualitative agreement between calculated and experimental results, is quite convincing.

(a)

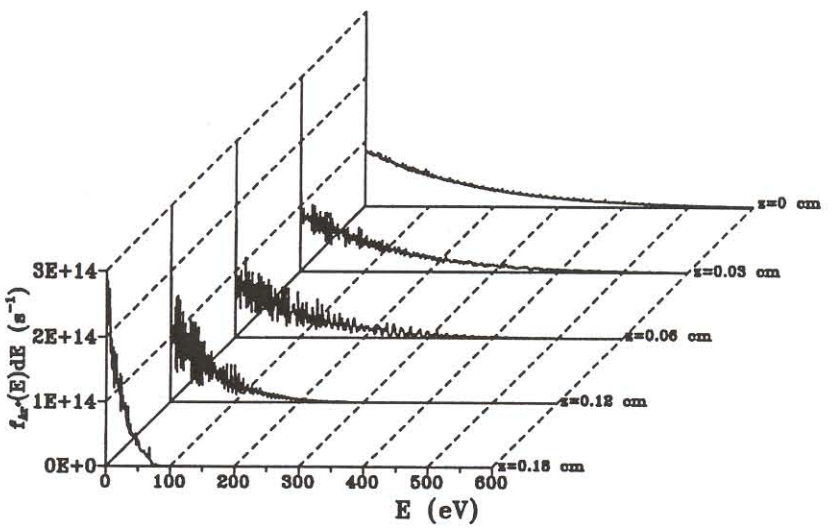

(b)

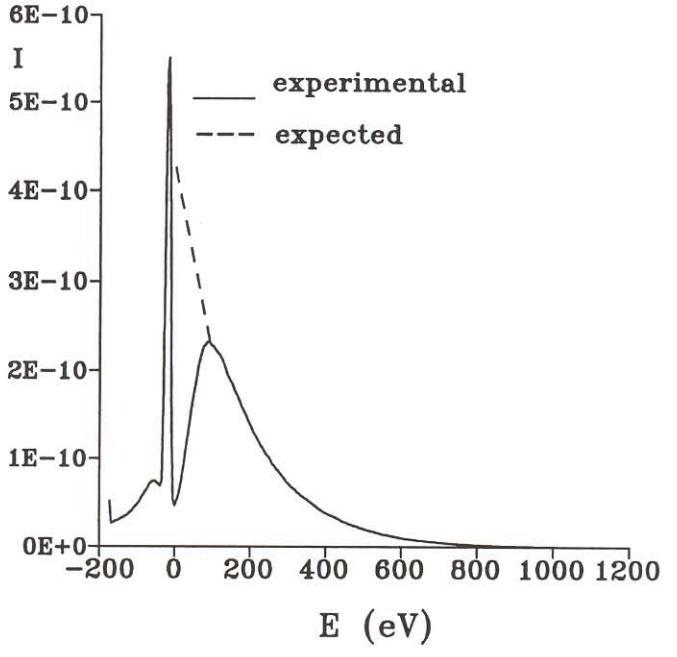

Figure 11: Flux energy distributions of the argon ions in a dc argon glow discharge: (a) calculated in the CDS, as a function of distance from the cathode, at a pressure of 75 Pa, a voltage of 1000 V and a current of 3.5 mA; (b) measured at the cathode, at 1000 V and 3 mA (pressure unknown). Reproduced from ref. 34 with permission of the Royal Society of Chemistry.

(a)

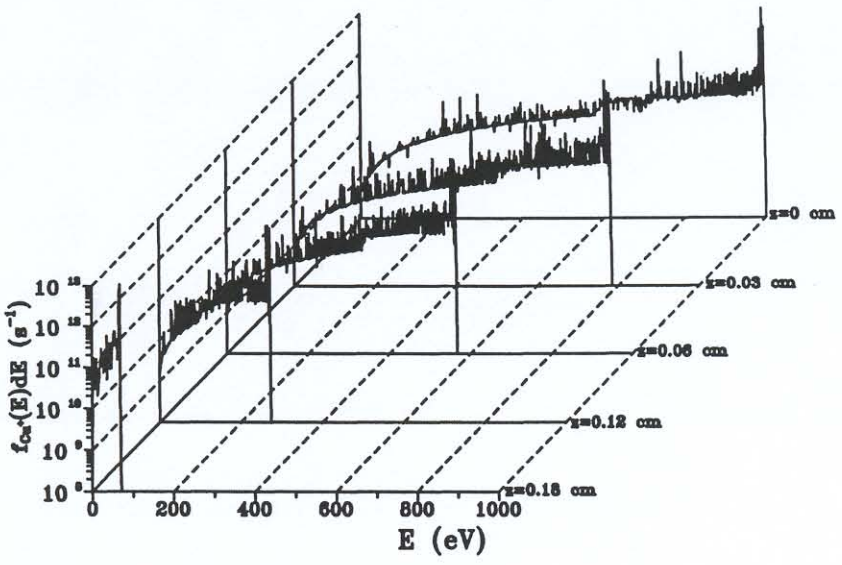

(b)

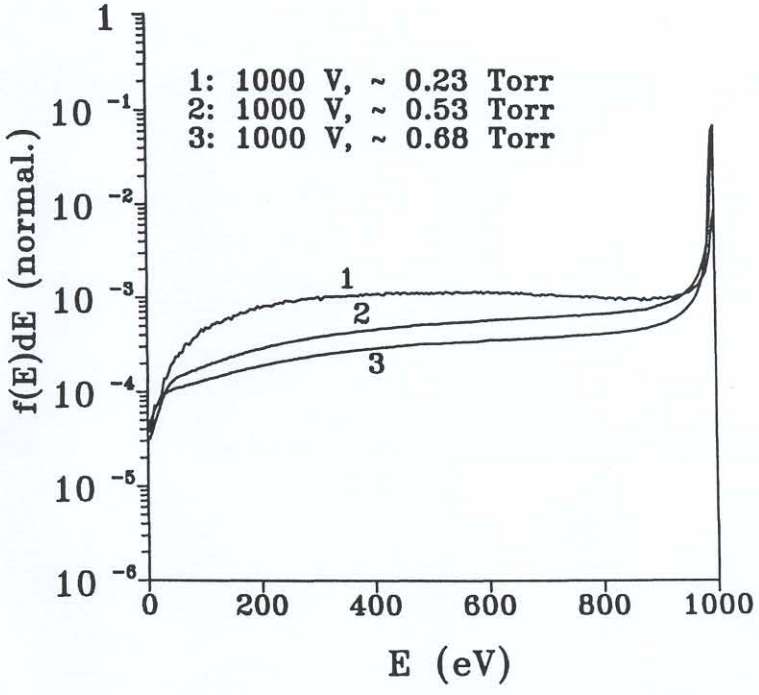

Figure 12: Flux energy distributions of the copper ions in a dc argon glow discharge: (a) calculated in the CDS, as a function of distance from the cathode, at a pressure of 75 Pa, a voltage of 1000 V and a current of 3.5 mA; (b) measured at the cathode, at 1000 V and three pressure values. Reproduced from ref. 34 with permission of the Royal Society of Chemistry.

3.5. Crater Profiles and Erosion Rates Due to Sputtering at the Cathode:

Based on the energy distributions of argon ions, fast argon atoms and copper ions bombarding the cathode, which are calculated in the Monte Carlo models, the flux of sputtered atoms can be calculated. Because the energy distributions are calculated in the models as a function of radial position, the sputtering flux as a function of radial position, and hence the cylindrically symmetrical two-dimensional crater profile after a certain period of sputtering, can be obtained. It should be mentioned that analytical glow discharges are often used for the depth-profiling analysis of layered materials. It is clear that in order to achieve a good depth resolution, the crater bottom should be very flat, so that atoms originating from the same depth are sputtered at the same time. However, this ideal situation is not always reached.

Figure 13a shows a typical experimental crater profile [37], obtained with a glow discharge ion source, which is not specifically designed for depth-profiling, but rather for the sensitive trace analysis of homogeneous samples. It is clear that this crater profile is not ideal for depth-profiling. Indeed, it is much deeper at the edges than in the center (so-called "crater edge effect"), the crater walls are not steep, and the crater bottom is not flat. Moreover, there is a small rim outside the crater profile, due to redeposition of sputtered atoms. This experimental crater profile is, however, also more or less found back in our model calculations, for the same discharge conditions and cell geometry, as can be seen in Figure 13b. Beside the qualitative agreement between calculated and experimental crater profiles, the absolute values of the Y-axis show that the results are also in satisfactory quantitative agreement. This example demonstrates that the model is able to make predictions about crater profiles to be expected for a specific cell geometry and certain discharge conditions. By applying some modifications to this geometry and/or to the discharge conditions, the crater profile could be optimized. In practice, this optimization procedure is commonly performed by trial-and-error. This can be expensive and time-consuming, and leads often to disappointing results. However, the optimization can now in principle also be simulated with the model, prior to building the new cell, which is much cheaper and more efficient.

It is also interesting to note that we have performed a comparison between calculated and measured erosion rates at the cathode due to sputtering, in a wide range of discharge conditions [38]. The results illustrated that excellent agreement was reached between model and experiment, both with respect to the absolute values, and to the variation of erosion rates as a function of voltage, pressure and current. This shows that the model can present a realistic picture of the sputtering process.

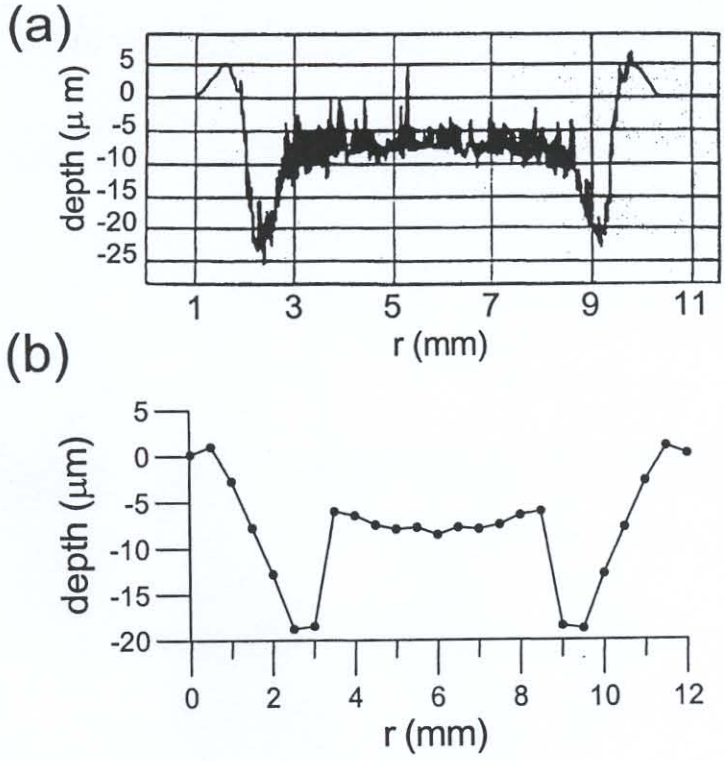

Figure 13: Crater profiles after 45 minutes of sputtering on a copper cathode, in a dc argon glow discharge: (a) measured at 1000 V and 3 mA (pressure unknown); (b) calculated at 1000 V, 75 Pa and 3.5 mA. Reproduced from ref. 34 with permission of the Royal Society of Chemistry.

3.6. Optical Emission Intensities:

Finally, from the collisional-radiative models which describe the behavior of various excited levels of argon atoms, copper atoms and copper ions, we were able to calculate optical emission intensities in the glow discharge, by multiplying the level populations with the Einstein transition probabilities for radiative decay.

We have calculated optical emission spectra, based on 605 ArI lines and 103 CuI and CuII lines. The results were in reasonable agreement with spectra found in the literature

[26]. Some specific ArI, CuI and CuII lines were also studied in more detail, as a function of discharge voltage and pressure, and the agreement between calculated and measured results, was fairly good [38]. Moreover, in order to study the relative importance of various excitation mechanisms, we have also compared calculated spectral line intensities, as a function of distance from the cathode, with measurements at exactly the same discharge conditions and cell geometry [39]. Figure 14a shows the calculated spatial distributions of two ArI lines, an ArII and a CuI line, at 80 Pa and five different currents and voltages. The corresponding experimental results [40] are plotted in figure 14b. It appears that the ArI 750.3 nm line, which originates from a high 4p level, shows a maximum in the beginning of the NG, due to electron impact excitation, as well as a minor peak near the cathode (in the so-called cathode glow, CG), attributed to fast argon ion and atom impact excitation. For the ArI 811.5 nm line, which originates from a low 4p level, the peak in the CG is higher than the peak in the NG. This tells us that high 4p levels are predominantly populated by electron impact excitation, which is generally accepted, but that for the low 4p levels the most important production process is ion and atom impact excitation, at the conditions under study here. The latter result is not so well-known, but it follows convincingly from the good agreement between the calculated and measured emission intensities as a function of distance from the cathode. The ArII lines are characterized by a peak in the NG, due to electron impact excitation. Indeed, for the argon ion excited levels, ion and atom impact excitation are not important, because the ion and atom energy which would be necessary to excite the ionic levels are much higher than the ion and atom energies typical for the glow discharge conditions under study. Finally, also the CuI lines are mainly characterized by a peak in the NG. This peak is rather broad for the CuI 324.7 nm line, as appears from figure 14. The reason is that this line is a resonant line (i.e., decaying to the ground state), which is subject to self-absorption [38]. In general, a very good agreement has been reached between the model calculations (figure 14a) and the corresponding experimental data (figure 14b), which suggests that our model takes into account the correct excitation mechanisms and uses realistic cross sections, and that it can therefore give more or less reliable predictions for GD-OES.

4. Conclusion

A comprehensive hybrid modeling network has been developed for argon glow discharges, including the sputtering of the copper cathode and the behavior of the copper atoms and ions. The main focus of this work was the description of glow discharges used in analytical spectrochemistry, operated in dc, capacitively coupled rf, and μs-pulsed mode. However, the model is also applicable to glow discharges operating at similar discharge conditions, but used for different application fields.

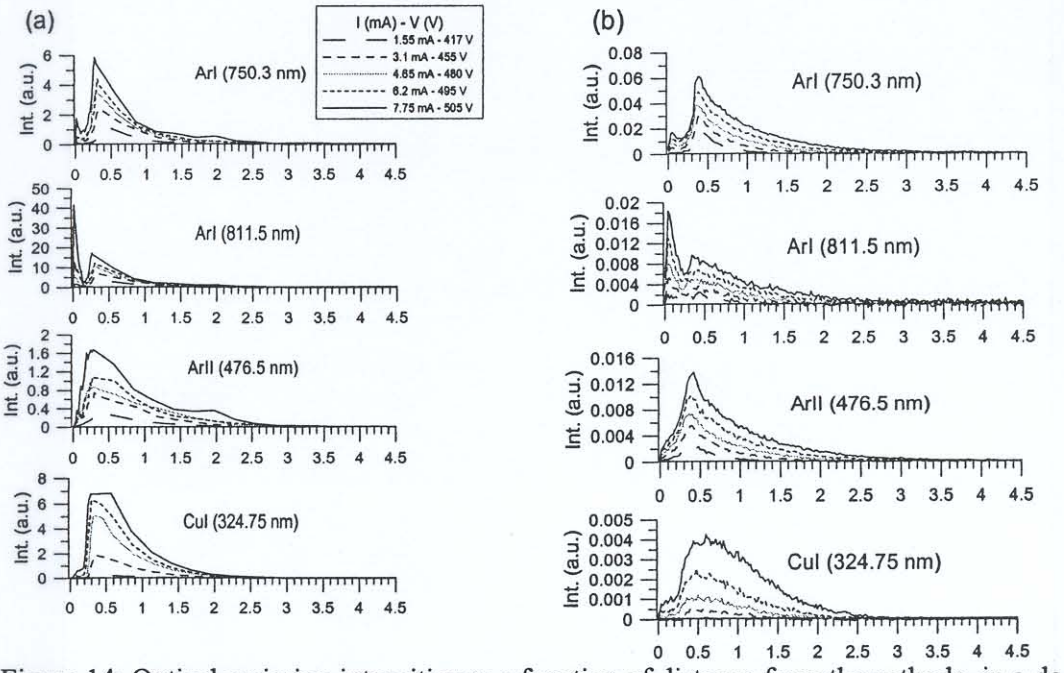

Figure 14: Optical emission intensities as a function of distance from the cathode, in a dc argon glow discharge, at a pressure of 80 Pa and five different currents and voltages, for the lines: ArI (750.3 nm), ArI (811.5 nm), ArII (476.5 nm) and CuI (324.75 nm). (a) calculated and (b) measured values [39].

The species described in the model include argon gas atoms, electrons, argon ions, fast argon atoms, argon atoms in various excited levels, sputtered copper atoms and the corresponding ions, both in the ground state and in various excited levels. These species are described with a combination of Monte Carlo, fluid, heat transfer and collisional-radiative models, which are all coupled to each other due to the interaction processes between the different species.

The typical results that have been obtained with the models, are summarized in this paper, and some illustrations are given, e.g., for the electrical characteristics, the potential distributions, the densities and energies of the various plasma species, as well as the crater profiles and erosion rates due to sputtering, and the optical emission intensities due to radiative decay of excited levels. The calculation results are compared with experimental data as much as possible, and the reasonable agreement between model and experiment shows that the model presents a realistic picture of the argon glow discharge with copper cathode.

Acknowledgments

A. Bogaerts is indebted to the Flemish Fund for Scientific Research (FWO) for financial support. This research is also sponsored by the Federal Services for Scientific, Technical and Cultural Affairs of the Prime Minister's Office (DWTC/SSTC) through

IUAP-IV (Conv. P4/10). Finally, we wish to thank W. Goedheer, J. Vlcek, R. Carman and V. Serikov for their valuable contributions to the development of this model network, and Z. Donko, V. Hoffmann, L. Wilken, W. W. Harrison, B. Smith, J. Winefordner, C. Jonkers and M. van Straaten for supplying the experimental data for comparison with the model results.

References:

1. A. Bogaerts, E. Neyts and R. Gijbels, Gas discharge plasmas and their applications, Spectrochim. Acta B Reviews, submitted.
2. R. K. Marcus, Glow Discharge Spectroscopies, Plenum Press, New York, 1993.
3. S. V. Berezhnoi, I. D. Kaganovich, L. D. Tsendin and V. A. Schweigert, Appl. Phys. Lett., 69 (1996) 2341-2343.
4. J. D. P. Passchier and W. J. Goedheer, J. Appl. Phys., 73 (1993) 1073-1079.
5. D. Loffhagen and R. Winkler, J. Comput. Phys., 112 (1994) 91-101.
6. Z. Donko, K. Rozsa and R. C. Tobin, J. Phys. D: Appl. Phys., 29 (1996) 105-114.
7. M. Surendra and D. B. Graves, IEEE Trans. Plasma Sci., 19 (1991) 144-157.
8. A. Bogaerts, R. Gijbels and V. V. Serikov, J. Appl. Phys., 87 (2000) 8334-8344.
9. A. Bogaerts, M. van Straaten and R. Gijbels, Spectrochim. Acta Part B, 50 (1995) 179-196.
10. A. Bogaerts, R. Gijbels and W. J. Goedheer, J. Appl. Phys., 78 (1995) 2233-2241.
11. A. Bogaerts, R. Gijbels and W. J. Goedheer, Jpn J. Appl. Phys., 38 (1999) 4404-4415.
12. M. Jogwich, B. A. Huber and K. Wiesemann, Z. Phys. D, 17 (1990) 171-179.
13. H. K. Gummel, IEEE Trans. Plasma Sci., 11 (1964) 455-465.
14. D. L. Scharfetter and H. K. Gummel, IEEE Trans. Electron. Devices, 16 (1969) 64-77.
15. A. Bogaerts and R. Gijbels, J. Appl. Phys., 86 (1999) 4124-4133.
16. A. Bogaerts and R. Gijbels, J. Appl. Phys., 78 (1995) 6427-6431.
17. A. Bogaerts and R. Gijbels, IEEE Trans. Plasma Sci., 27 (1999) 1406-1415.
18. T. Holstein, Phys. Rev. 83 (1951) 1159-1168.
19. P. J. Walsh, Phys. Rev., 116 (1959) 511-515.
20. A. Bogaerts, R. Gijbels and J. Vlcek, J. Appl. Phys., 84 (1998) 121-136.
21. N. Matsunami, Y. Yamamura, Y. Itikawa, N. Itoh, Y. Kazumata, S. Miyagawa, K. Morita, R. Shimizu and H. Tawara, Atom. Data Nucl. Data Tables, 31 (1984) 1-80.
22. A. Bogaerts, M. van Straaten and R. Gijbels, J. Appl. Phys., 77 (1995) 1868-1874.
23. A. Bogaerts, R. Gijbels and R. J. Carman, Spectrochim. Acta Part B, 53 (1998) 1679-1703.
24. A. Bogaerts and R. Gijbels, J. Appl. Phys., 79 (1996) 1279-1286.
25. F. W. Aston, Proc. Royal Soc. London, Ser. A, 79 (1907) 80.
26. A. Bogaerts, R. Gijbels and J. Vlcek, Spectrochim. Acta Part B, 53 (1998) 1517-1526.
27. W. Vieth and J. C. Huneke, Spectrochim. Acta Part B, 46 (1991) 137-153.

28. A. Bogaerts and R. Gijbels, J. Anal. At. Spectrom., 15 (2000) 895-905.
29. A. Bogaerts, A. Quentmeier, N. Jakubowski and R. Gijbels, Spectrochim. Acta Part B, 50 (1995) 1337-1349.
30. A. Bogaerts and R. Gijbels, Spectrochim. Acta Part B, 53 (1998) 437-462.
31. E. B. M. Steers and R. J. Fielding, J. Anal. At. Spectrom., 2 (1987) 239-244.
32. A. Bogaerts, E. Wagner, B. W. Smith, J. D. Winefordner, D. Pollmann, W. W. Harrison and R. Gijbels, Spectrochim. Acta Part B, 52 (1997) 205-218.
33. A. Bogaerts, R. D. Guenard, B. W. Smith, J. D. Winefordner, W. W. Harrison and R. Gijbels, Spectrochim. Acta Part B, 52 (1997) 219-229.
34. A. Bogaerts and R. Gijbels, J. Anal. At. Spectrom., 13 (1998) 945-953.
35. H. D. Hagstrum, Phys. Rev., 96 (1954) 325-335.
36. M. van Straaten, A. Bogaerts and R. Gijbels, Spectrochim. Acta Part B, 50 (1995) 583-605.
37. C. Jonkers, Ph. D. Dissertation, University of Antwerp, 1995.
38. A. Bogaerts, L. Wilken, V. Hoffmann, R. Gijbels and K. Wetzig, Spectrochim. Acta Part B, in press.
39. A. Bogaerts, Z. Donko, K. Kutasi, G. Bano, N. Pinhao and M. Pinheiro, Spectrochim. Acta Part B, 55 (2000) 1465-1479.
40. Z. Donko, G. Bano, L. Szalai, K. Kutasi, K. Rosza, M. Pinheiro and N. Pinhao, J. Phys. D: Appl. Phys., 32 (1999) 2416-2425.